frontiers | Frontiers in Earth Science

ORIGINAL RESEARCH
published: 05 April 2022
doi: 10.3389/feart.2022.880692

Quantitative Evaluation of Coseismic Deformations Induced by Seismogenic Faulting in Mining Exploration Area During the 2018 Xingwen and 2019 Changning Earthquakes, Sichuan, China

Chunwei Sun[1], Sixiang Ling[1], Siyuan Zhao[2], Hong Wen[1] and Sen Wang[1]*

[1]Faculty of Geosciences and Environmental Engineering, Southwest Jiaotong University, Chengdu, China, [2]State Key Laboratory of Hydraulics and Mountain River Engineering, College of Water Resources and Hydropower, Sichuan University, Chengdu, China

OPEN ACCESS

Edited by:
Xiangjun Pei,
Chengdu University of Technology, China

Reviewed by:
Jing Luo,
Northwest Institute of Eco-Environment and Resources (CAS), China
Zain Maqsood,
National University of Sciences and Technology (NUST), Pakistan
Dao-Yuan Tan,
Hong Kong Polytechnic University, Hong Kong SAR, China

***Correspondence:**
Siyuan Zhao
zhaosiyuan@scu.edu.cn

Specialty section:
This article was submitted to Geohazards and Georisks, a section of the journal Frontiers in Earth Science

Received: *21 February 2022*
Accepted: *17 March 2022*
Published: *05 April 2022*

Citation:
Sun C, Ling S, Zhao S, Wen H and Wang S (2022) Quantitative Evaluation of Coseismic Deformations Induced by Seismogenic Faulting in Mining Exploration Area During the 2018 Xingwen and 2019 Changning Earthquakes, Sichuan, China. Front. Earth Sci. 10:880692. doi: 10.3389/feart.2022.880692

In the period between December 2018 and July 2019, a series of earthquakes (EQs), including the 16 December 2018 Ms 5.7 Xingwen mainshock and the 17 June 2019 Ms 6.0 Changning mainshock, struck the Changning shale gas exploration field in the southern margin of the Sichuan Basin. The Xingwen and Changning EQs both occurred on concealed faults, which led to hundreds of casualties, and affected a total of over 160 thousand people in southern Sichuan. The aftershock sequences following the Xingwen and Changning EQs were clustered in the vicinity of the Jianwu syncline and Changning anticline, respectively, and occurred mostly at depths of 3–7 km. In this study, coseismic surface deformation measurements obtained through differential interferometric synthetic aperture radar (D-InSAR) data were used to identify the faulting geometries and distributions. The coseismic deformation maps have maximum line-of-sight (LOS) displacements of ~4.53 cm on the northwest side of the Xingwen EQ source fault and ~7.84 cm on the southwest side of the Changning EQ source fault. The calculated static Coulomb stress changes indicated that most aftershocks occurred in increasing stress zones following the mainshock ruptures. From the InSAR deformation field, a complicated concealed seismogenic doublet fault was inferred, which predominately exhibited left-lateral strike-slip motion during the Xingwen and Changning EQs. The footwall ramp of the basement fault reactivated first, and resulted in the Xingwen EQ and concentrating stresses beneath the Changning anticline, which induced the Changning EQ half a year later. Compared with previous studies, we proposed that the fault network was lubricated by water that was injected during shale gas exploration, facilitating the occurrence of the Xingwen and Changning EQs. Such work evaluated the coseismic deformations of the Xingwen and Changning EQs, and derived the regional faulting distribution from aftershock sequences. It could provide useful information for monitoring and analyzing seismic activity around the hinge zones of folds in mining exploration areas, which contributes to effective risk assessment of disasters associated with seismic geo-environments.

Keywords: eathquake, coseismic deformation, mining exploration area, D-InSAR, seismogenic fault

INTRODUCTION

In the period between December 2018 and July 2019, two major earthquakes (EQs) with aftershocks, namely, the Xingwen and Changning EQs, struck southern Yibin city, Sichuan Province, where is situated in the southern margin of the Sichuan Basin (**Figure 1A**; **Table 1**). The magnitudes Ms of the mainshocks were 5.7 and 6.0, respectively. China Earthquake Networks Centre (https://data.earthquake.cn) recorded 10 Ms > 3 aftershocks (the largest is a Ms 5.3 event) followed the Xingwen EQ, and 68 Ms > 3 aftershocks (the largest is a Ms 5. 3 event) followed the Changning EQ. Preliminary teleseismic waveform analyses suggested that the rupture processes responsible for the Xingwen and Changning EQs occurred on concealed strike-slip faults (e.g., Yi et al., 2019; Yin et al., 2019; Liu and Zahradník, 2020). On the other hand, previous studies performed on the Changning-Gongxian region and around Yibin city have revealed earthquakes induced by water injection (e.g., Sun et al., 2017; Lei et al., 2017; Lei et al., 2019a), seismic hazards triggered by hydraulic fracturing (e.g.,

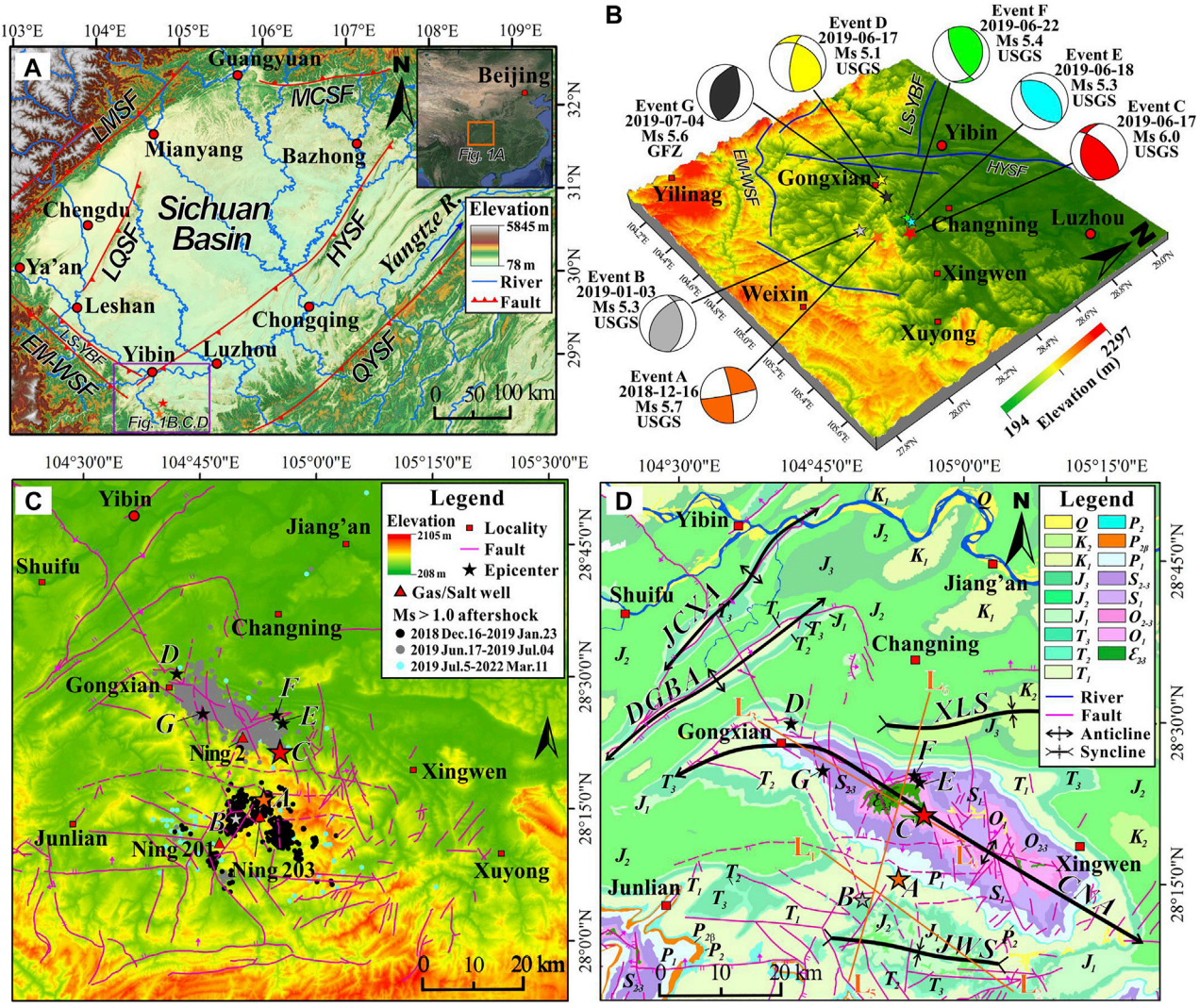

FIGURE 1 | (A) Simplified topographical and tectonic map of the Sichuan Basin. *MCSF*: Micangshan fault; *LMSF*: Longmenshan fault; *LQSF*: Longquanshan fault; *HYSF*: Huayingshan fault; *QYSF*: Qiyaoshan fault; *EM-WSF*: Emei-Washan fault; *LS-YBF*: Leshan-Yibin fault. **(B)** Topographic map and focal mechanism solutions of the Ms 5.7 Xingwen mainshock (Event A, orange star) with its largest aftershock (Event B, grey star) and the Ms 6.0 Changning mainshock (Event C, red star) with its Ms > 5.0 aftershocks (Events D-G, other stars). **(C)** Topography and EQ information with faults in the study area. Stars indicate the epicenters of Events A-G. The dark, gey, and light blue dots refer to the Ms > 1.0 aftershocks (Lei et al., 2019a; Hu et al., 2020; Long et al., 2020; CENC, 2022). Fault data are derived from a 1:200,000 geological map and Long et al. (2020). **(D)** Geological map. CNA, Changning anticline; DGBA, Dengganba anticline; JCXA, Jiacunxi anticline; JWS, Jianwu syncline; XLS, Xiangling syncline. Q, Quaternary; K_2, Upper Cretaceous; K_1, Lower Cretaceous; J_3, Upper Jurassic; J_2, Middle Jurassic; J_1, Lower Jurassic; T_3, Upper Triassic; T_2, Middle Triassic; T_1, Lower Triassic; P_2, Upper Permian; $P_{2\beta}$, Upper Permian Emeishan basalt; P_1, Lower Permian; $S_{2\text{-}3}$, Middle to Upper Silurian; S_1, Lower Silurian; $O_{2\text{-}3}$, Middle to Upper Ordovician; O_1, Lower Ordovician; $\epsilon_{2\text{-}3}$, Middle to Upper Cambrian. Profiles L_1–L_2 and L_3–L_4 are displayed in **Figure 6**, and Profile L_5–L_6 is displayed in **Figure 7**.

TABLE 1 | Earthquake parameters that were used in this study.

Event	EQ name	Ms	Shock	Date (yy-mm-dd)	Time (UTC+8)	Latitude (°)	Longitude (°)	Depth (km)
A	"12.16" Xingwen EQ	5.7	Mainshock	2018-12-16	12:46:07	N28.24	E104.92	12
B	"1.3" Gongxian EQ	5.3	Afterschock	2019-01-03	08:48:06	N28.20	E104.86	15
C	"6.17" Changning EQ	6.0	Mainshock	2019-06-17	22:55:43	N28.34	E104.96	10[a]
D	"6.17" Gongxian EQ	5.1	Afterschock	2019-06-17	23:36:01	N28.47	E104.72	11.5[a]
E	"6.18" Changning EQ	5.3	Afterschock	2019-06-18	07:34:33	N28.39	E104.95	10[a]
F	"6.22" Gongxian EQ	5.5	Afterschock	2019-06-22	22:29:56	N28.40	E104.94	10
G	"7.4" Gongxian EQ	5.6	Afterschock	2019-07-04	10:17:58	N28.40	E104.78	8

Note: The data are quoted from China Earthquake Networks Center (CENC, 2022).

[a]*These depths are from German Research Centre for Geosciences (GFZ). Ms is the surface wave magnitude.*

TABLE 2 | Focal mechanism solutions for "12.16" Xingwen and "6.17" Changning EQs.

EQs	Source	Magnitude	Depth (km)	Fault plane 1			Fault plane 2		
				Strike (°)	Dip (°)	Rake (°)	Strike (°)	Dip (°)	Rake (°)
Xingwen	USGS[a]	Mw 5.3	17.5	80	87	−173	349	83	−3
	GFZ[b]	Mw 5.3	26	246	70	−166	359	77	−21
	Yi[c]	Ms 5.7	3	80	85	−166	349	76	−5
Changning	USGS[a]	Mw 5.8	11.5	314	65	62	185	37	135
	GFZ[b]	Mw 5.8	10	315	61	53	192	46	137
	Yi[c]	Ms 6.0	3	131	51	36	16	63	135
	HU[d]	Mw 5.7	12	323	57	65	184	40	123

[a]*USGS, United States Geological Survey*

[b]*GFZ, German Research Centre for Geosciences*

[c]*Yi = Yi et al. (2019)*

[d]*HU, Harvard University*

Mw is the moment magnitude; Ms is the surface wave magnitude.

Hu et al., 2018; He et al., 2019) and the three-dimensional velocity structure and faulting styles (e.g., Lei et al., 2019b; Liu and Zahradník, 2020; Long et al., 2020). The focal mechanism solutions for the Xingwen and Changning EQs, each of which produced a series of Ms > 5.0 aftershocks (**Figure 1B**), were provided from the U.S. Geological Survey (abbr. USGS) and the German Research Centre for Geosciences (abbr. GFZ) (**Table 2**). However, the seismogenic faults responsible for these two major EQs have not been identified or studied in detail. Field investigations were carried out immediately after the Xingwen and Changning EQs, but no obvious surface ruptures were found. Owing to the complex topography and dense coverage of vegetation in the EQ-impacted source regions, it is difficult to determine the geometric and kinematic characteristics of the seismogenic faults, and their relationships with nearby active faults is unknow. These problems constitute great significance for understanding the tectonic activity and seismogenic trends in this region, which would be helpful for preventing and controlling coseismic geo-hazards in the southern margin of the Sichuan Basin.

Fortunately, the interferometric synthetic aperture radar (InSAR) deformation fields produced by the Xingwen and Changning EQs are highly beneficial for a better understanding the motions and properties of the seismogenic faults. The two major EQs with a series of Ms >5.0 aftershocks thereby provide a good opportunity to study the seismic activity of the region and the relationship between seismogenic fault and coseismic deformation in the southern margin of the Sichuan Basin. In this particular case, the InSAR analysis is highly helpful to obtain the coseismic displacement field, that will improve our understanding of faulting in the region. The InSAR technique has been extensively and successfully applied to determine the coseismic displacements of EQs, especially megathrust EQs (Simons et al., 2002; Biggs et al., 2006; Zuo et al., 2016; Wang et al., 2017; Zhao et al., 2018). Meanwhile, differential interferometric synthetic aperture radar (D-InSAR), based on radar satellite synthetic aperture radar (SAR) imagery, has emerged as an indispensable tool to measure the millimetre-scale deformation of the Earth's surface (Stramondo et al., 2011; Syahreza et al., 2018) produced by a wide variety of natural phenomena, such as earthquakes, volcanic eruptions, land subsidence (Bonì et al., 2017; Aguirre et al., 2018; Sarychikhina et al., 2018; Zhao et al., 2018; Su et al., 2019), ice sheet and glacier movements (Liao et al., 2018), and landslides (Raspini et al., 2017; Carlà et al., 2019). Regional-scale surface deformation can be measured by D-InSAR technique with a high

sensitivity, which is useful to detect coseismic deformation generated by concealed seismogenic faulting.

In this study, the ascending InSAR observations was used to provide robust constraints on the location of the seismogenic fault and coseismic deformation, from which we can deduce the mechanisms of seismogenic faults. We first described the regional faults, including the Mabian-Yanjian fault, the Zhaotong-Lianfeng fault, and the Huayingshan fault (**Figure 1A**), in the Yibin region. Then, two pairs of ascending orbit Sentinel-1A (S1A) SAR images covering the periods of Xingwen and Changning EQs occurrence were used for D-InSAR processing. The coseismic deformation and seismogenic faults were analyzed, and a geostructural model with an EQ sequence was proposed. This study aspires to achieve three objectives: 1) to explore the coseismic surface deformation generated by the Xingwen and Changning EQs, 2) to characterize the seismogenic faults for the two EQs, and 3) to reveal the regional kinematics of these seismogenic faults and their tectonic implications from the perspective of a geostructural model with an EQ sequence. The study region could present a case study of the seismogenic mechanism responsible for earthquakes with magnitudes less than 6.0 that frequently occur within the subparallel EW-trending Yunnan-Guizhou fold belt in the southern margin of the Sichuan Basin. This investigation could thereby provide information crucial for ascertaining that the Xingwen and Changning EQ sequences in the Jianwu syncline and the Changning anticline were probably caused by long-term hydraulic fracturing.

GEOLOGICAL AND EARTHQUAKE SETTINGS

Regional Geology

A concentrated series of earthquake events struck Changning, Gongxian, and Xingwen Counties, which are situated approximately 5–10 km SE of Yibin city, between December 2018 and July 2019 (**Figures 1A,B**; **Table 1**). Tectonically, the study area is situated in the transition zone (i.e., the junction) between the Sichuan Basin in the upper Yangtze quasi-Platform and the Yunnan-Guizhou fold belt, which is located in the southern margin of the Sichuan Basin (**Figure 1A**; Sun et al., 2017). Structurally, regional faults are well developed and are characterized by the dominant NE-trending Huayingshan fault zone, the NW-trending Emei-Washan fault zone, and the NW-trending Leshan-Yibin fault. In particular, the study area is located in the southern junction between the Huayingshan and Emei-Washan fault zones (**Figures 1A,B**).

The study region is nestled atop a tectonic alpine landform with an elevation ranging from 208 to 2,105 m above sea level (**Figure 1C**). This region is dominated by the Triassic and Cretaceous sedimentary rocks, with a few units from the Cambrian, Ordovician, Silurian, and Permian periods (**Figure 1D**). The Silurian, Jurassic and Cretaceous strata mainly consist of sandstone and siltstone interlayered with mudstone. The Triassic outcrops comprise sandstone with shale (T_3), limestone and dolomite (T_2), and siltstone, flysch layers of mudstone, shale and sandstone (T_1). The Cambrian, Ordovician, and Permian outcrops are composed mostly of limestone and dolomite interlayered with shale, sandstone, or siltstone, while the upper Permian stratum includes the Emeishan basalt ($P_{2\beta}$). The crystalline basement of the Sichuan Basin is roughly bounded by the Huayingshan fault zone (Li et al., 2015). The basement comprises rigid granite in the west at depths of 3–6 km and weakly metamorphosed rocks (which are relatively plastic) in the east at depths of 6–9 km (Zhou et al., 1997). The basement depth in the northeastern Yibin area ranges from 7.0 to 13.0 km, while that of southwestern Yibin is less than 5.0 km, reflecting a slope of the crystalline basement (Li et al., 2018; Wang et al., 2018b). The geological structures in the study area exhibits numerous anticlines (i.e., the Jiacunxi, Dengganba, and Changning anticlines) in addition to the Jianwu and Xiangling synclines (**Figure 1D**). The Changning anticline, which trends NW-SE, extends through Gongxian in the NW to the Xuyong area in the SE. The core of the Changning anticline exposes the Cambrian system, and the surrounding strata successively expose the Ordovician, Silurian, Permian, Triassic, and Jurassic; in the south, the Jianwu syncline is exposed with the Jurassic constituting its core strata (**Figure 1D**). The study area boasts abundant shale gas resources (e.g., Ning 201, Ning 203, shown in **Figure 1C**) in the Changning shale gas field and salt mine (e.g., Ning 2, shown in **Figure 1C**), and these resources are widely exploited by hydraulic fracturing through the water injection method (Sun et al., 2017; Lei et al., 2017, 2019).

Earthquake Setting

Two major EQs struck southern Yibin city between December 2018 and July 2019, resulting in a series of aftershocks (Ms > 5) that affected the entire study area (**Figures 1B,C**), as described in **Table 1**. The first mainshock occurred at 12:46 p.m. local time on 16 December 2018 with a magnitude of Ms 5.7, which resulted in a seismic intensity of VII on the Modified Mercalli scale (CENC, 2022). Its epicenter was located at 28.24°N, 104.92°E (Xingwen County) with a focal depth of 12 km; this event is known as the "12.16" Xingwen EQ (Event A, **Table 1**; **Figures 1B–D**). The "12.16" Xingwen EQ caused damage to more than 500 buildings and 17 injuries (CENC, 2022), and an aftershock occurred on 3 January 2019 with a magnitude of Ms 5.3 (Event B, **Table 1**; **Figures 1B–D**). The Xingwen EQ occurred on a fault located between the Changning anticline and Jianwu syncline, while the aftershocks were located primarily to the south of the Xingwen mainshock and around the Jianwu syncline (**Figures 1C,D**).

The second mainshock occurred at 22:53 p.m. local time on 17 June 2019 with a magnitude of Ms 6.0, which resulted in a seismic intensity of VIII on the Modified Mercalli scale (CENC, 2022). Its epicenter was located at 28.34°N, 104.96°E (Changning County) with a focal depth of 10 km; this event is known as the "6.17" Changning EQ (Event C, **Table 1**; **Figures 1B–D**). The "6.17" Changning EQ caused damage to more than 1,000 buildings, took the lives of 13 people, and injured 226 others (CENC, 2022). The epicenter of the "6.17" Changning mainshock was approximately 15 km from the mainshock of the "12.16" Ms 5.7 Xingwen EQ. Four of the aftershocks, which all had magnitudes greater than 5 (Ms 5.1, Ms 5.3, Ms 5.4, and Ms 5.6 in chronological order),

TABLE 3 | Parameters of the Sentinel-1A pairs that were used in this study (A is ascending orbit).

No.	Acquisition time	Path No.	Azi. angle	Perp.B(m)	Incidence (°)	EQ event
Xingwen EQ	20181204-20181216	128 (A)	−168.13	10	43.92	A
Channing EQ	20190609-20190621	55 (A)	−167.44	11	33.90	C/D/E

occurred from 17 June to 4 July 2019 (Events D, E, F and G, respectively, **Table 1**; **Figures 1B–D**). The epicenter of the Changning EQ mainshock and its aftershocks were located mostly within the Changning anticline (**Figure 1D**).

MATERIALS AND METHODS

InSAR Data

The coseismic deformation field is fundamental for analyzing the intensity and seismogenic mechanism of an earthquake. However, the low number of ground GPS stations deployed in the Yibin area has heretofore made it difficult to measure the coseismic deformation field by conventional crustal deformation observation techniques (e.g., Simons et al., 2002; Anzidi et al., 2009). Therefore, SAR images have become important data for deriving the coseismic deformation field. To isolate the coseismic surface deformation induced by a series of EQs in the Yibin area, we used SAR data acquired before and after the two events by the Sentinel-1A (S1A) satellite. S1A carries a C-band microwave sensor that runs in Terrain Observation by Progressive Scans (TOPS) mode and boasts a large spatial coverage (i.e., 250 km) with a repeat time of 12 days (Attema et al., 2008; Geudtner et al., 2014). S1A SAR data have been extensively applied to monitor coseismic deformation fields with a short revisit period, a high orbit accuracy, and high-altitude interferograms in vegetation-covered areas (e.g., Zuo et al., 2016; Zhao et al., 2018; Kovács et al., 2019). We downloaded S1A SAR images covering the entire study area acquired before and after the EQs for the analysis. Field investigations suggested that the rupture did not break the surface, and descending orbit data are characterized by low-quality observations; thus ascending data are more suitable for this task (e.g., Zhao et al., 2018). Therefore, two pairs of ascending orbit S1A single look complex (SLC) images were employed to constrain the coseismic deformation of the Xingwen and Changning EQs. The detailed parameters of the S1A data were described in **Table 3**. The SLC images were all produced in Interferometric Wide (IW) swath mode. The pixel spacing in the slant range and azimuth directions are 2.33 and 13.93 m, respectively.

Interferogram Processing

The traditional two-pass differential interferometric method with the burst-by-burst processing approach was used to process the S1A SAR images before and after each EQ, from which the interferometric phase could be obtained (e.g., Hanssen, 2001). First, SLC bursts were co-registered using precise orbit data in conjunction with 30-m resolution digital elevation model (DEM) data taken from the Advanced Land Observing Satellite digital surface model (ALOS DSM) AW3D30 (https://www.eorc.jaxa.jp/ALOS/en/aw3d30). Using the same DEM covering the study area to remove the residual topographic component, D-InSAR interferograms were calculated for each burst with multilook factors of 2.33 and 13.93 m pixels in the azimuth and range directions, respectively. Third, using the enhanced spectral diversity method, which is often applied for along-track interferometry in regions where successive bursts overlap in the azimuth direction, the residual azimuth phase ramp (attributable to possible azimuth mis-registration) was compensated. Finally, we projected the unwrapped 30-m-resolution data from the satellite azimuth, and calculated the deformation values for the investigated areas, with the range coordinate converted into Universal Transverse Mercator (UTM) coordinates (e.g., He et al., 2018). In addition, to obtain a better deformation phase, the phase effects caused by errors due to thermal and atmospheric noise and orbit errors were removed (e.g., Goldstein and Werner, 1998; Hanssen, 2001; Liu et al., 2016).

Coulomb Failure Stress Calculation

The static Coulomb failure stress (CFS) change induced by an EQ was used to assess the potential of future seismicity after the Xingwen and Changning EQs. The dislocation model combined with the CFS model (Okada, 1985) was used to evaluate the static CFS changes in the surrounding regions following the Xingwen and Changning EQs. The CFS change is estimated from the earthquake source model using the Coulomb failure stress criterion, as described as follows:

$$\Delta CFS = \Delta\tau_s + \mu'\Delta\sigma_n$$

where ΔCFS denotes the CFS change along the receiver fault, $\Delta\tau_s$ is the change in the shear stress in the fault slip direction, μ' denotes the effective friction coefficient of the receiver fault, and $\Delta\sigma_n$ is the change in the normal stress on the receiving fault plane.

In the following calculations, changes in the shear stress $\Delta\tau_s$ on a receiver fault are positive, and $\Delta\sigma_n$ is positive for an increasing clamping normal stress, where pressure is defined as positive value. According to previous studies (e.g., Lin and Stein, 2004; Toda et al., 2005, 2011), μ' varies from 0.1 to 0.4 for faults with considerable cumulative slip or high pore pressure, and varies from 0.4 to 0.8 for faults with little cumulative slip. In this study, an effective friction coefficient of 0.4 was adopted for the analysis, which is the mean value within the range suitable for continental strike-slip faults (Toda et al., 2005). Young's modulus and Poisson's ratio were set to 8×10^5 bar and 0.25, respectively. The Coulomb 3.3 software, developed by the USGS (Toda et al.,

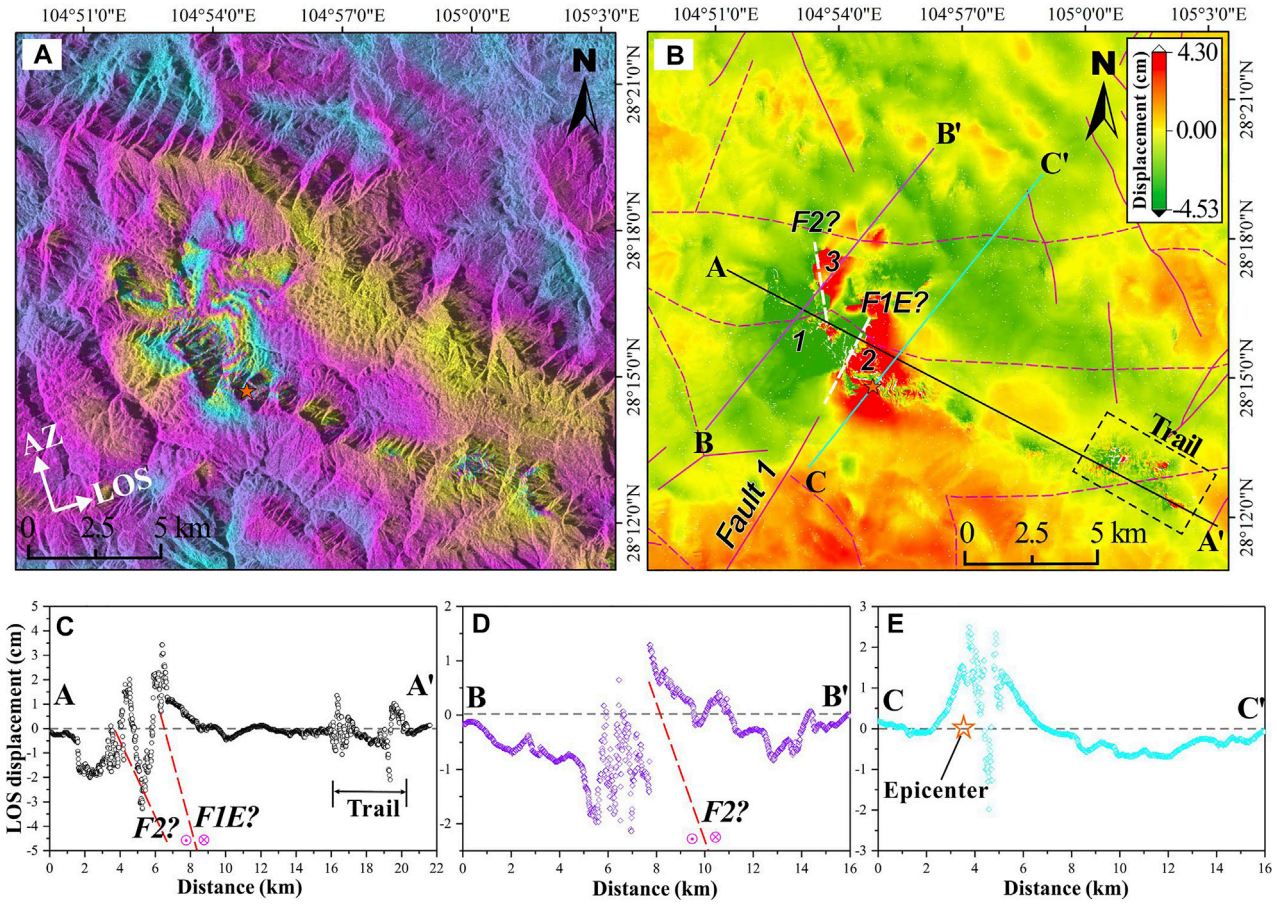

FIGURE 2 | Coseismic deformation field of the "12.16" Ms 5.7 Xingwen earthquake. **(A)** Sentinel-1A ascending interferograms. **(B)** Coseismic displacement field from Sentinel-1A ascending oribit InSAR data. The maximum positive and negative LOS displacements are 4.30 and 4.53cm, respectively. **(C**,**D**,**E)** Line-of-sight (LOS) displacements in the ascending InSAR measurements along Profile A–A′ **(C)**, Profile B–B′ **(D)**, and Profile C–C′ **(E)** in **(B)**. The orange star represents the epicenter of the Ms 5.7 Xingwen earthquake. F1 and F2: Faults 1 and 2, respectively; F1E: Extension of Fault 1.

2005, 2011), was applied to calculate the CFS changes. The results of CFS changes denote the average changes adjacent to the fault.

RESULTS

The D-InSAR ascending orbit interferograms and coseismic deformation maps revealed clear interferometric fringes caused by the Xingwen and Changning EQs (**Figures 2–4**). The high coherence was mainly attributable to the sparse vegetation coverage, whereas the low coherence was primarily caused by atmospheric errors. Meanwhile, the low coherence was also influenced by the temporal and geometrical distortions in the areas of steep terrain and dense vegetation. The total displacement along the line-of-sight (LOS) direction of an InSAR interferogram largely depended on the contributions of the east-west and up-down components, which was constructively or destructively interfered on the two sides of a seismogenic fault. As shown in these figures, the Xingwen and Changning EQs caused subsidence, which was accompanied by some horizontal deformation.

Coseismic Deformation by the "12.16" Xingwen EQ

The D-InSAR interferograms and deformation maps of the "12.16" Xingwen EQ (**Figure 2**) showed some incoherent regions in the near-field region of the seismogenic fault but clear interferometric fringes. The whole displacement field, which covered an area of approximately 10 × 10 km^2, exhibited periodicity with a butterfly-shaped fringe distribution (**Figure 2A**). Moreover, a "trail" was observed ~8 km to the SE of the Xingwen EQ epicenter (**Figures 2A,B**). The LOS deformation in the ascending deformation map ranged from −4.53 to 4.30 cm. We also plotted three profiles (oriented NW, NE, and NE) across the main coseismic deformation field (**Figures 2C–E**). The epicenter, located along the southeastern boundary of the coseismic deformation field, exhibited a small and generally negligible displacement (nearly 0 cm, **Figure 2C**). Profiles A–A′ and B–B′ (NW- and NE-trending cross-sections, respectively, across the inferred seismogenic fault)

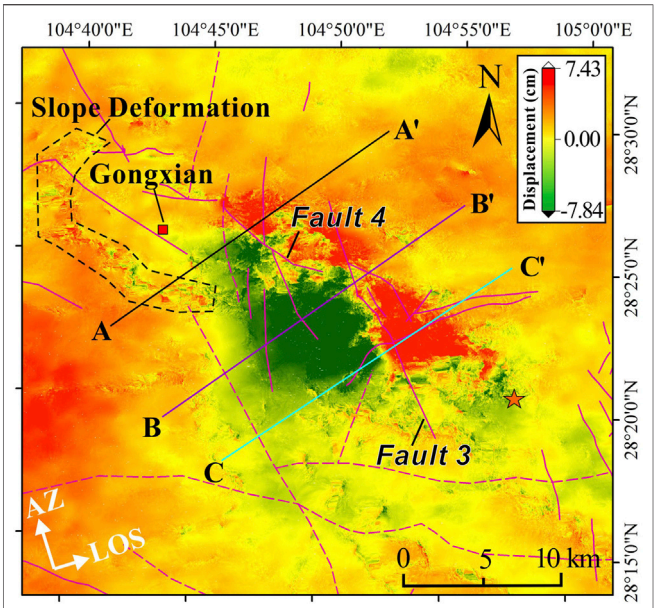

FIGURE 3 | Coseismic displacement field caused by the "6.17" Ms 6.0 Changning earthquake from Sentinel-1A ascending orbit InSAR data. The maximum positive and negative LOS displacements are 7.43 and 7.84 cm, respectively.

displayed LOS displacement curves with maximum differential displacements of ~8 and ~3.5 cm, respectively (**Figures 2C,D,E**). Additionally, the abovementioned trail of displacement had a range of ~2 cm along the ridge (**Figure 2C**). We speculated that this deformation occurred near ridges, which probably resulted from the amplification of displacement by seismic waves (e.g., Havenith et al., 2003; Meunier et al., 2008; Li et al., 2019). Profile C–C′ displayed a positive displacement (**Figure 2E**), indicating uplift of the east wall.

The LOS deformation field displayed an anomaly with two dissociated positive displacement zones (Zones 2 and 3). We inferred that this anomaly resulted from two major concealed faults (Faults 1 and 2) that ruptured during the Xingwen EQ (**Figure 2B**). Although negative displacement fields were distributed to the west and northeast of Zones 2 and 3, they were clustered mainly in Zone 1 (**Figure 2B**). Therefore, the fringes and displacements were asymmetric across the source fault striking subparallel to the north, implying two concealed rupture faults (Faults 1 and 2) in a direction subparallel to the north across the coseismic displacement field. Negative displacements were presented in the ascending deformation map for the west wall of the fault, while positive displacements were observed for the east wall of the fault, constituting the left-lateral strike-slip motion. This discovery was consistent with previous knowledge from the focal mechanism solution of the mainshock (**Figure 1B**; **Table 2**), which indicated that the "12.16" Xingwen EQ predominantly demonstrated strike-slip motion. However, these D-InSAR measurements revealed two major rupture processes (along Faults 1 and

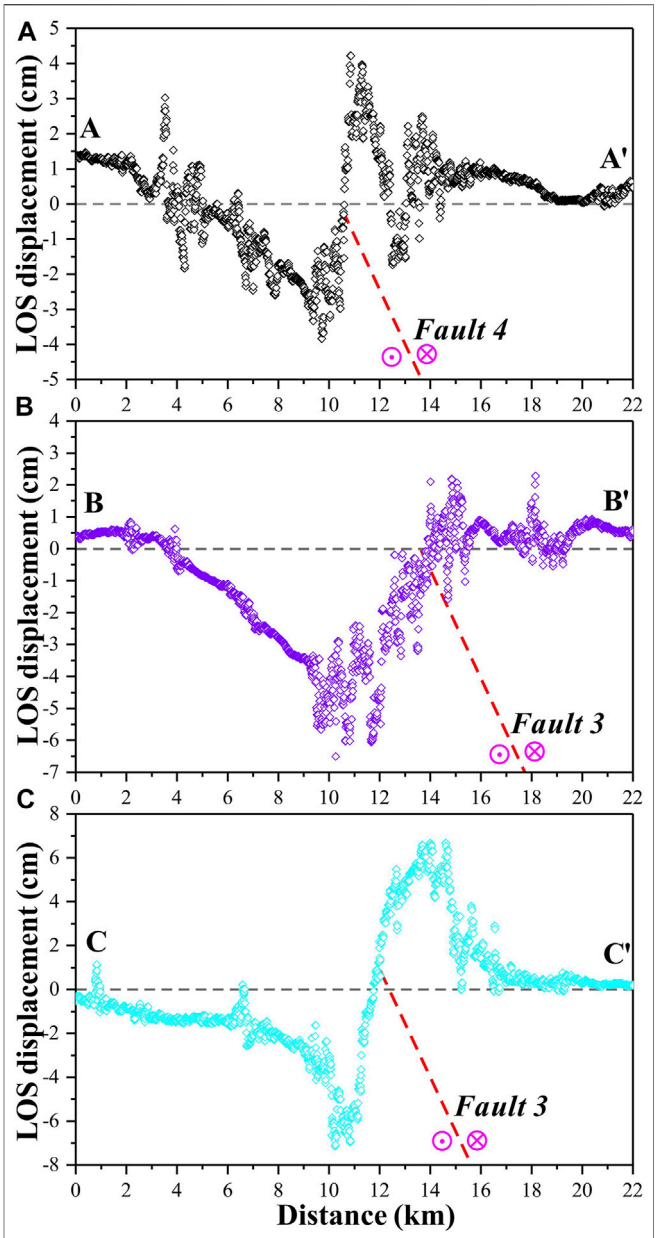

FIGURE 4 | Line-of-sight (LOS) displacements in the ascending InSAR measurements along multiple profiles. **(A)** LOS displacements along Profile A–A′. **(B)** LOS displacements along Profile B–B′. **(C)** LOS displacements along Profile C–C′. The locations of Profiles A–A′, B–B′, and C–C′ are shown in **Figure 3**.

2) during the Xingwen EQ. According to the geological structural feature (**Figures 1C,D**), it could be deduced that the coseismic deformation fields of the Xingwen EQ were primarily generated from the rupture of Fault 1, and were also contributed from the displacement of Fault 2 that was driven by the former Fault 1. It suggested that left-lateral strike-slip deformation was induced by complicated seismogenic structures, as was also reported by Gong et al. (2019).

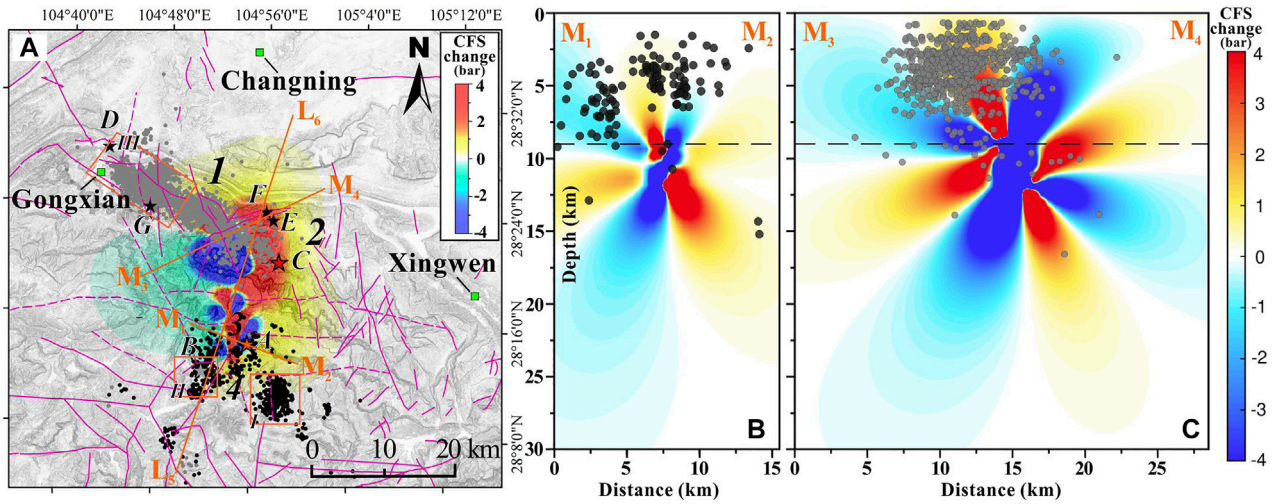

FIGURE 5 | Coulomb failure stress (CFS) changes in the study area. **(A)** CFS change at a depth of 9 km. **(B,C)** CFS changes on Profiles M_1–M_2 and M_3–M_4, which are labeled in **(A)**. Stars denote the epicenters of the Ms > 5 aftershocks. Dark and grey dots represent the epicenters of the Ms > 1 aftershocks of the Xingwen and Changning earthquakes, respectively. The cross-section of Profile L_5–L_6 is presented in **Figure 7**.

Coseismic Deformation by the "6.17" Changning EQ

The coseismic deformation maps of the "6.17" Changning EQ from the D-InSAR measurements are shown in **Figure 3**. The whole coseismic displacement field, which covered an area of approximately 20 × 15 km^2, displayed a rectangular distribution with a NW-trending long side. The LOS displacements in the ascending deformation map ranged from -7.84 to 7.43 cm. The epicenter, located along the southeastern margin of the coseismic deformation field, featured a small, negligible displacement (approximately 0 cm). The maximum difference between the maximum positive and negative displacements was approximately 15 cm, which is located near the speculated seismogenic fault approximately 4 km NW of the epicenter. The northwest direction of epicentre, there has a clear signal, which probably caused by the topographic and remained atmospheric errors (**Figure 3**).

The clear deformation fields were asymmetric across the source fault striking along the NW, implying a NW-trending seismogenic fault bisecting the coseismic displacement field (**Figure 3**). Three NE-trending profiles were constructed across the northern, middle, and southern portions of the inferred seismogenic fault (**Figure 4**). The maximum displacements reached ~4.5 cm, ~6.5 cm, and ~7 cm on Profiles A–A′, B–B′, and C–C′, respectively (**Figures 4A–C**). All three components of the fault displaced an analogous tangential curve along the cross-sections, resulting in negative displacements on the southwestern sides of Faults 3 and 4. Meanwhile, positive displacements were discovered in the ascending deformation map for the east wall of the fault, while corresponding negative displacements were found for the west wall, constituting left-lateral strike-slip movement. Therefore, Fault 3 was identified as the inferred seismogenic fault from the coseismic displacement field established by the InSAR data. This hypothesis was in agreement with previous focal mechanism solutions. The focal mechanism solution of the mainshock revealed that the "6.17" Changning EQ displayed left-lateral strike-slip movement with a minor component of over-thrusting motion (**Figure 1B**; **Table 2**), which is also supported by Yi et al. (2019). However, coseismic displacements also clearly occurred along Fault 4. Hence, we proposed that Fault 4 have simultaneously ruptured with Fault 3, which accorded with the concealed seismogenic doublet that formed during the Changning EQ reported by Liu and Zahradník (2020).

Changes in the Coulomb Failure Stress

The Coulomb failure stress changes (ΔCFS) on the surrounding faults after a mainshock play an important role in triggering subsequent earthquakes within seismic zones (e.g., Freed, 2005; Wang et al., 2018a; Zhao et al., 2018; Cui et al., 2021). Here we combined the Xingwen and Changning EQs to illustrate the CFS changes in **Figure 5**. The ΔCFS at a depth of 9 km was calculated (**Figure 5A**) for the receiver faults: a strike of 349°, dip of 83° and rake of -3° for the Xingwen EQ, and a strike of 314°, dip of 65° and rake of 62° for the Changning EQ. **Figure 5A** shows that there are four positive (stress increase) ΔCFS areas marked as Zones 1, 2, 3, and 4. Large ΔCFS increases were mostly concentrated around the inferred seismogenic faults. Evidently, most aftershocks correlated very well with increases in the ΔCFS. Moreover, ~80% of the aftershocks following the Changning EQ occurred to the NW of the Changning mainshock with increasing ΔCFS in Zone 1 (**Figure 5A**), whereas ~60% of the Xingwen aftershocks were clustered to the SW and SE of the Xingwen mainshock with increasing ΔCFS in Zone 4 (**Figure 5A**). Furthermore, we constructed three

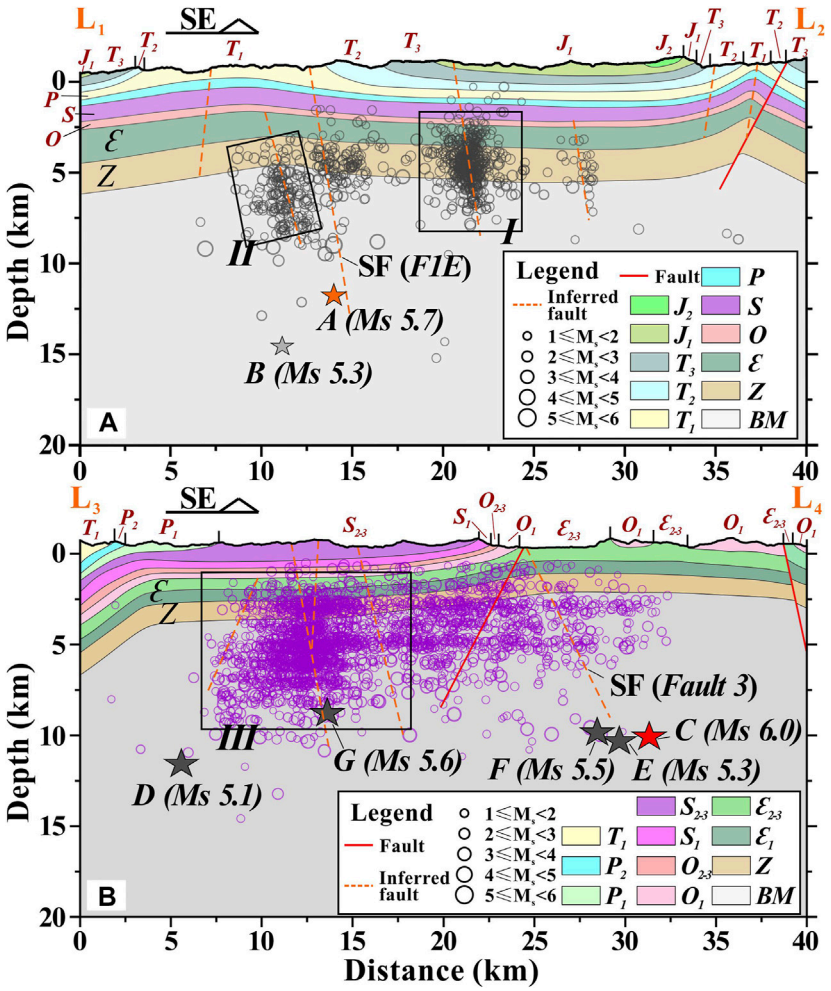

FIGURE 6 | Geological sections with faults laid atop the projected earthquakes within 5 km of Profiles L_1–L_2 and L_3–L_4 in **Figure 1D**. The geological sections were drawn based on a 1:200,000 geological map. SF: Seismogenic fault; BM: Proterozoic and Archaeozoic basement.

cross-sections across the inferred seismogenic fault segment, as shown in **Figure 5A**. Three negative ΔCFS lobes were recognized on Profile M_1–M_2 as a result of the Xingwen EQ, and more than ~60% of the aftershocks occurred in these decreasing ΔCFS zones (**Figure 5B**). However, four positive ΔCFS lobes were identified across the inferred seismogenic fault as a result of the Changning EQ, and ~70% of the corresponding aftershocks were clustered in increasing ΔCFS zones (**Figure 5C**). The cross-sections in **Figures 5B,C** demonstrated that the aftershocks were clustered at depths of 2–7 km, which were shallower than the fault plane responsible for the mainshock. These ΔCFS calculations indicated that the Xingwen and Changning mainshocks induced stresses and promoted seismicity on the surrounding fault network. Hence, ~80% of the Xingwen aftershocks occurred on the surrounding faults, which were clustered in the SE (Zone I) and SW (Zone II), ~70% of the aftershocks following the Changning EQ occurred on the NW fault network in Zone III (**Figure 5A**).

DISCUSSION

The velocity structure and fault network of the study area have been partly identified by Long et al. (2020), but many faults have yet to be found or verified within this complicated fault network. The concealed seismogenic faults responsible for the Xingwen and Changning EQs was in proximity to many surrounding faults, which raised essential questions about the relationship and interaction among these faults. Nevertheless, the relationship and interaction between the seismogenic faults and the surrounding fault network in the investigated area remain unknown. Our findings indicated that the seismogenic faults responsible for the Xingwen and Changning EQs are concealed strike-slip faults. We identified the seismogenic fault of the Xingwen EQ as the NE extension of the northern segment of Fault 1, because the InSAR-derived surface trace of the seismogenic fault and the aftershock distribution were consistent with this interpretation (**Figure 2B**). Moreover, the rupture of Fault 1 resulted in the deformation of a secondary fault

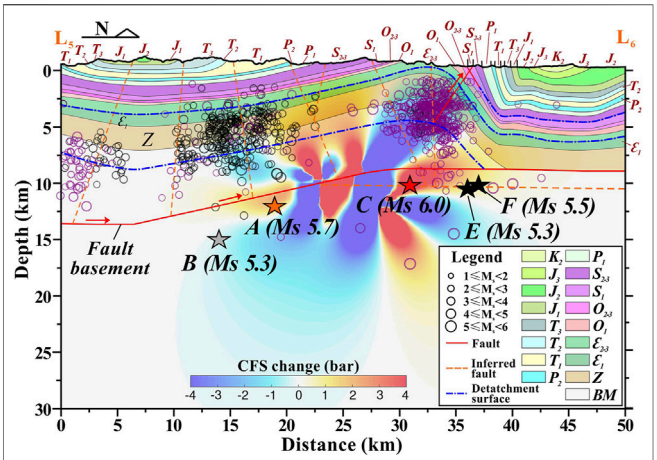

FIGURE 7 | Tectonic geological sections (Profile L_5–L_6 in **Figures 1D**, **5A**) with projected earthquakes within 5 km laid atop the Coulomb failure stress changes along Profile L_5–L_6. The geological sections were drawn based on a 1:200,000 geological map and He et al. (2019). BM: Proterozoic and Archaeozoic basement.

of Fault 2, which led to the coseismic surface deformation on both sides of Fault 2. The seismogenic fault responsible for the Changning EQ was identified as Fault 3 by the coseismic displacement changes around its southwestern and northeastern sides (**Figure 3A**). Although many aftershocks were clustered around the extensions of Faults 1 and 3, many aftershocks were also concentrated in Zones I and II during the Xingwen EQ and in Zone III during the Changning EQ (**Figure 5A**).

The source depth and distribution characteristics can be implied by projecting the aftershock locations. The aftershock projections onto the geological sections of Profiles L_1–L_2, L_3–L_4, and L_5–L_6 are illustrated in **Figures 6**, **7**. The hypocentres of the aftershocks following the Xingwen and Changning EQs were distributed mostly at depths of 2–10 km. We identified the inferred concealed faults from the sequences of hypocentres; clusters could be clearly distinguished in Zones I and II during the Xingwen EQ, and a vague cluster can be detected in Zone III during the Changning EQ (**Figures 5A**, **6**). The structural model in **Figure 7** depicted the tectonic setting that facilitated the occurrence of earthquakes across the Jianwu syncline and the Changning anticline. The Xingwen and Changning mainshocks were projected onto the break in the basement fault ramp, indicating that most of the aftershocks were shallower than the two mainshocks. Furthermore, the hypocentres of the aftershocks following the Xingwen and Changning EQs were relatively concentrated within the hinge zones of the Jianwu syncline and the Changning anticline, respectively (**Figure 7**). The earthquake cluster locations reflected the shear behavior between the strata layer and the shear failure of the faulted basement, which resulted in the Xingwen and Changning EQs. The calculated ΔCFS values also reflected shear failure of the faulted basement, and the crustal stress was also concentrated along the axes of the Jianwu syncline and Changning anticline.

We propose an interpretation where the fault basement was initially reactivated as a result of shear failure due to the Xingwen EQ located between the Jianwu syncline and the Changning anticline, which resulted in the concentration of stress under the Changning anticline. Thereafter the fault basement fractured along the hinge zone of the Changning anticline, which subsequently led to the Changning EQ half a year following the Xingwen EQ. According to previous studies (e.g., Sun et al., 2017; Lei et al., 2019a, 2019b), the increase in seismic activity (mostly Ms < 5.0) over the last ~10 years was induced by hydraulic fracturing in the Changning gas exploration field, where the hypocentres were concentrated mostly at depths of 3–7 km. The hypocentres of the Xingwen and Changning aftershocks were also likely facilitated by elevated pore pressures due to the injection of water over the past ~10 years into gas wells and salt mine wells (e.g., Ning 201, Ning 203 and Ning 2, **Figure 1C**). In other words, the fault network was lubricated by water that was injected during shale gas exploration. Then, crustal stresses became concentrated within the hinge zones of the Jianwu syncline and Changning anticline, which resulted in the Xingwen EQ near the Jianwu syncline and the Changning EQ beneath the Changning anticline. Meanwhile, the injection of water also led to clusters of seismic activity in Zones I and II in the Jianwu syncline and Zone III NW of the Changning anticline (**Figures 5A**, **6**).

CONCLUSION

We investigated the coseismic deformation associated with the 2018 Xingwen and 2019 Changning EQs using S1A data. Evident coseismic displacements were identified on both sides of the seismogenic faults responsible for the Xingwen EQ (December 2018) and the Changning EQ (June 2019) according to the InSAR imagery. The InSAR observations demonstrated the concealed seismogenic doublet with left-lateral strike-slip motion for the Xingwen and Changning EQs and an apparent thrust-slip component for the Changning EQ. The aftershock hypocentres were mostly shallower than 10 km; the Xingwen aftershocks were predominantly clustered in the Jianwu syncline, whereas the Changning aftershocks were mostly clustered in the Changning anticline. The faulted basement was first sheared along a ramp, resulting in the Xingwen EQ; then, the crustal stresses became concentrated in the basement beneath the Changning anticline, resulting in the Changning EQ half a year later. The Xingwen and Changning EQs probably resulted from long-term hydraulic fracturing during shale gas exploration; consequently, the clusters of seismic activity in the hinge zones of the abovementioned folds need to be further monitored and analyzed in the future. The D-InSAR analysis on seismic deformations produced by seismogenic faulting could arouse the understanding of seismic geo-environment in similar mining exploration areas, which is helpful for assessing disaster risks associated with earthquakes.

DATA AVAILABILITY STATEMENT

The original contributions presented in the study are included in the article/Supplementary Material, further inquiries can be directed to the corresponding author.

AUTHOR CONTRIBUTIONS

SZ and SL conceptualized the research, and contributed to data analysis and investigation. CS contributed to the study methodology and the writing of the original draft. HW and SW contributed the field surveys and draft modification. All authors have agreed the publication of the manuscript.

FUNDING

This study is financially supported by the National Natural Science Foundations of China (Nos 41907228; 42007248), the Second Tibetan Plateau Scientific Expedition and Research Program (No. 2019QZKK0905), the Sichuan Science and Technology Program (No. 2020YFS0297), and the Sichuan Science and Technology Innovation and Seeding Cultivation (No. 2021086).

ACKNOWLEDGMENTS

We would like to thank the European Space Agency (ESA) for providing the satellite data used in this paper. We also thank Xiaohui Hu from the Institute of Disaster Prevention, Feng Long from Seismological Bureau of Sichuan Province, and Xinlin Lei from Geological Survey of Japan share the aftershock location data.

REFERENCES

Aguirre, P., Vásquez, J., de la Llera, J. C., González, J., and González, G. (2018). Earthquake Damage Assessment for Deterministic Scenarios in Iquique, Chile. *Nat. Hazards* 92, 1433–1461. doi:10.1007/s11069-018-3258-3

Anzidei, M., Boschi, E., Cannelli, V., Devoti, R., Esposito, A., Galvani, A., et al. (2009). Coseismic Deformation of the Destructive April 6, 2009 L'Aquila Earthquake (central Italy) from GPS Data. *Geophys. Res. Lett.* 36, L17307. doi:10.1029/2009GL039145

Attema, E., Davidson, M., Floury, N., and Levrini, G. (2008). "Sentinel-1 ESA's New European Radar Observatory," in *European Conference on Synthetic Aperture Radar VDE*. Friedrichshafen, Germany: VDE, 1–4.

Biggs, J., Bergman, E., Emmerson, B., Funning, G. J., Jackson, J., Parsons, B., et al. (2006). Fault Identification for Buried Strike-Slip Earthquakes Using InSAR: the 1994 and 2004 Al Hoceima, Morocco Earthquakes. *Geophys. J. Int.* 166, 1347–1362. doi:10.1111/j.1365-246X.2006.03071.x

Bonì, R., Meisina, C., Cigna, F., Herrera, G., Notti, D., Bricker, S., et al. (2017). Exploitation of Satellite A-DInSAR Time Series for Detection, Characterization and Modelling of Land Subsidence. *Geosciences* 7, 25. doi:10.3390/geosciences7020025

Carlà, T., Intrieri, E., Raspini, F., Bardi, F., Farina, P., Ferretti, A., et al. (2019). Perspectives on the Prediction of Catastrophic Slope Failures from Satellite InSAR. *Sci. Rep.* 9, 14137. doi:10.1038/s41598-019-50792-y

CENC (2022). China Earthquake Networks Center. Sichuan Earthquake Administration, China Earthquake Administration. Available at: http://www.eqsc.gov.cn.

Cui, S., Pei, X., Jiang, Y., Wang, G., Fan, X., Yang, Q., et al. (2021). Liquefaction within a Bedding Fault: Understanding the Initiation and Movement of the Daguangbao Landslide Triggered by the 2008 Wenchuan Earthquake (Ms = 8.0). *Eng. Geology*. 295, 106455. doi:10.1016/j.enggeo.2021.106455

Freed, A. M. (2005). Earthquake Triggering by Static, Dynamic, and Postseismic Stress Transfer. *Annu. Rev. Earth Planet. Sci.* 33, 335–367. doi:10.1146/annurev.earth.33.092203.122505

Geudtner, D., Torres, R., Snoeij, P., Davidson, M., and Rommen, B. (2014). Sentinel-1 System Capabilities and Applications. *IEEE Geosci. Remote Sensing Symp.* 2014, 1457–1460. doi:10.1109/IGARSS.2014.6946711

Goldstein, R. M., and Werner, C. L. (1998). Radar Interferogram Filtering for Geophysical Applications. *Geophys. Res. Lett.* 25, 4035–4038. doi:10.1029/1998GL900033

Gong, Y., Zhao, M., Long, F., and Fu, Y. (2019). Precise Relocation of Aftershock Sequence of Xingwen M5.7 Earthquakes on December 16, 2018. *Earthquake Res. Sichuan* 172, 1–5. (in Chinese with English Abstract). doi:10.13716/j.cnki.1001-8115.2019.03.001

Hanssen, R. F. (2001). *Radar Interferometry: Data Interpretation and Error Analysis (308pp)*. Netherlands: Kluwer Academic Publishers.

Havenith, H.-B., Vanini, M., Jongmans, D., and Faccioli, E. (2003). Initiation of Earthquake-Induced Slope Failure: Influence of Topographical and Other Site Specific Amplification Effects. *J. Seismology* 7, 397–412. doi:10.1023/a:1024534105559

He, D., Lu, R., Huang, H., Wang, X., Jiang, H., and Zhang, W. (2019). Tectonic and Geological Setting of the Earthquake Hazards in the Changning Shale Gas Development Zone, Sichuan Basin, SW China. *Pet. Exploration Development* 46, 1051–1064. doi:10.1016/S1876-3804(19)60262-4

He, P., Hetland, E. A., Niemi, N. A., Wang, Q., Wen, Y., and Ding, K. (2018). The 2016 Mw 6.5 Nura Earthquake in the Trans Alai Range, Northern Pamir: Possible Rupture on a Back-Thrust Fault Constrained by Sentinel-1A Radar Interferometry. *Tectonophysics* 749, 62–71. doi:10.1016/j.tecto.2018.10.025

Hu, J., Chen, J., Chen, Z., Cao, J., Wang, Q., Zhao, L., et al. (2018). Risk Assessment of Seismic Hazards in Hydraulic Fracturing Areas Based on Fuzzy Comprehensive Evaluation and AHP Method (FAHP): a Case Analysis of Shangluo Area in Yibin City, Sichuan Province, China. *J. Pet. Sci. Eng.* 170, 797–812. doi:10.1016/j.petrol.2018.06.066

Hu, X., Sheng, S., Wan, Y., Bu, Y., and Li, Z. (2020). Study on Focal Mechanism and post-seismic Tectonic Stress Field of the Changning, Sichuan, Earthquake Sequence on June 17th 2019. *Process Geophys. (in Chinese)* 35 (5), 1657–1681. doi:10.6038/pg2020DD0378

Kovács, I. P., Bugya, T., Czigány, S. z., Defilippi, M., Lóczy, D., Riccardi, P., et al. (2019). How to Avoid False Interpretations of Sentinel-1A TOPSAR Interferometric Data in Landslide Mapping? A Case Study: Recent Landslides in Transdanubi, Hungary. *Nat. Hazards* 96, 693–712. doi:10.1007/s11069-018-3564-9

Lei, X., Huang, D., Su, J., Jiang, G., Wang, X., Wang, H., et al. (2017). Fault Reactivation and Earthquakes with Magnitudes of up to Mw4.7 Induced by Shale-Gas Hydraulic Fracturing in Sichuan Basin, China. *Sci. Rep.* 7, 7971. doi:10.1038/s41598-017-08557-y

Lei, X., Wang, Z., and Su, J. (2019a). The December 2018 ML 5.7 and January 2019 ML 5.3 Earthquakes in South Sichuan Basin Induced by Shale Gas Hydraulic Fracturing. *Seismological Res. Lett.* 90, 1099–1110. doi:10.1785/0220190029

Lei, X., Wang, Z. W., Wang, Z., and Su, J. (2019b). Possible Link between Long-Term and Short-Term Water Injections and Earthquakes in Salt Mine and Shale Gas Site in Changning, South Sichuan Basin, China. *Earth Planet. Phys.* 3, 510–525. doi:10.26464/epp2019052

Li, B., Song, Y. B., Wang, Q., Wang, Z. B., Guo, L., Jiang, J. M., et al. (2018). Magnetic Field Characteristics and Geological Significance of Sichuan basin. *Geophys. Geochemical Exploration* 42, 937–945. (in Chinese with English Abstract). doi:10.11720/wtyht.2018.1527

Li, C., He, D., Sun, Y., He, J., and Jiang, Z. (2015). Structural Characteristic and Origin of Intra-continental Fold belt in the Eastern Sichuan basin, south China Block. *J. Asian Earth Sci.* 111, 206–221. doi:10.1016/j.jseaes.2015.07.027

Li, X.-n., Ling, S.-x., Sun, C.-w., Xu, J.-x., and Huang, T. (2019). Integrated rockfall hazard and Risk Assessment along Highways: an Example for Jiuzhaigou Area after the 2017 Ms 7.0 Jiuzhaigou Earthquake, China. *J. Mt. Sci.* 16, 1318–1335. doi:10.1007/s11629-018-5355-x

Liao, H., Meyer, F. J., Scheuchl, B., Mouginot, J., Joughin, I., and Rignot, E. (2018). Ionospheric Correction of InSAR Data for Accurate Ice Velocity Measurement at Polar Regions. *Remote Sensing Environ.* 209, 166–180. doi:10.1016/j.rse.2018.02.048

Lin, J., and Stein, R. S. (2004). Stress Triggering in Thrust and Subduction Earthquakes and Stress Interaction between the Southern San Andreas and

Nearby Thrust and Strike-Slip Faults. *J. Geophys. Res.* 109, B02303. doi:10.1029/2003JB002607

Liu, G., Song, R., Guo, H., Perski, Z., Yue, H., Han, C., et al. (2016). Filtering SAR Interferometric Phase Noise Using a Split-Window Model. *Remote Sensing Lett.* 7, 800–809. doi:10.1080/2150704x.2016.1187316

Liu, J., and Zahradník, J. (2020). The 2019 M W 5.7 Changning Earthquake, Sichuan Basin, China: A Shallow Doublet with Different Faulting Styles. *Geophys. Res. Lett.* 47, e2019GL085408. doi:10.1029/2019GL085408

Long, F., Zhang, Z. W., Zhang, Z., Qi, Y., Liang, M., Ruan, X., et al. (2020). Three Dimensional Velocity Structure and Accurate Earthquake Location in Changning-Gongxian Area of Southeast Sichuan. *Earth Planet. Phys.* 4, 1–15. doi:10.26464/epp2020022

Meunier, P., Hovius, N., and Haines, J. A. (2008). Topographic Site Effects and the Location of Earthquake Induced Landslides. *Earth Planet. Sci. Lett.* 275, 221–232. doi:10.1016/j.epsl.2008.07.020

Okada, Y. (1985). Surface Deformation Due to Shear and Tensile Faults in a Half-Space. *Bull. Seismological Soc. America* 75 (4), 1135–1154. doi:10.1785/bssa0750041135

Raspini, F., Bardi, F., Bianchini, S., Ciampalini, A., Del Ventisette, C., Farina, P., et al. (2017). The Contribution of Satellite SAR-Derived Displacement Measurements in Landslide Risk Management Practices. *Nat. Hazards* 86, 327–351. doi:10.1007/s11069-016-2691-4

Sarychikhina, O., Glowacka, E., and Robles, B. (2018). Multi-sensor DInSAR Applied to the Spatiotemporal Evolution Analysis of Ground Surface Deformation in Cerro Prieto basin, Baja California, Mexico, for the 1993-2014 Period. *Nat. Hazards* 92, 225–255. doi:10.1007/s11069-018-3206-2

Simons, M., Fialko, Y., and Rivera, L. (2002). Coseismic Deformation from the 1999 Mw 7.1 Hector Mine, California, Earthquake as Inferred from InSAR and GPS Observations. *Bull. Seismological Soc. America* 92, 1390–1402. doi:10.1785/0120000933

Stramondo, S., Chini, M., Bignami, C., Salvi, S., and Atzori, S. (2011). X-, C-, and L-Band DInSAR Investigation of the April 6, 2009, Abruzzi Earthquake. *IEEE Geosci. Remote Sensing Lett.* 8, 49–53. doi:10.1109/lgrs.2010.2051015

Su, Z., Yang, Y.-H., Li, Y.-S., Xu, X.-W., Zhang, J., Zhou, X., et al. (2019). Coseismic Displacement of the 5 April 2017 Mashhad Earthquake (Mw 6.1) in NE Iran through Sentinel-1A TOPS Data: New Implications for the Strain Partitioning in the Southern Binalud Mountains. *J. Asian Earth Sci.* 169, 244–256. doi:10.1016/j.jseaes.2018.08.010

Sun, X., Yang, P., and Zhang, Z. (2017). A Study of Earthquakes Induced by Water Injection in the Changning Salt Mine Area, SW China. *J. Asian Earth Sci.* 136, 102–109. doi:10.1016/j.jseaes.2017.01.030

Syahreza, S., Fadhli, A., Saepuloh, A., and Lateh, H. (2018). Combining the Sentinel-1A/B DinSAR Interferometry to Detect Deformation Associated with Pidie Jaya Earthquake. *J. Phys. Conf. Ser.* 1120, 012021. doi:10.1088/1742-6596/1120/1/012021

Toda, S., Stein, R. S., Richards-Dinger, K., and Bozkurt, S. B. (2005). Forecasting the Evolution of Seismicity in Southern California: Animations Built on Earthquake Stress Transfer. *J. Geophys. Res.* 110, B05S16. doi:10.1029/2004JB003415

Toda, S., Stein, R. S., Sevilgen, V., and Lin, J. (2011). "Coulomb 3.3 Graphic-Rich Deformation and Stress-Change Software for Earthquake, Tectonic, and Volcano Research and Teaching-User Guide," in *U.S. Geological Survey Open-File Report*, 63. 2011–1060, Available at: https://pubs.usgs.gov/of/2011/1060/, Accessed date: March 2018. doi:10.3133/ofr20111060

Wang, H., Liu-Zeng, J., Ng, A. H.-M., Ge, L., Javed, F., Long, F., et al. (2017). Sentinel-1 Observations of the 2016 Menyuan Earthquake: A Buried Reverse Event Linked to the Left-Lateral Haiyuan Fault. *Int. J. Appl. Earth Observation Geoinformation* 61, 14–21. doi:10.1016/j.jag.2017.04.011

Wang, L., Gao, H., Feng, G., and Xu, W. (2018a). Source Parameters and Triggering Links of the Earthquake Sequence in central Italy from 2009 to 2016 Analyzed with GPS and InSAR Data. *Tectonophysics* 744, 285–295. doi:10.1016/j.tecto.2018.07.013

Wang, Z. J., Wang, H. C., Dong, D., and Qin, J. (2018b). Review of Geophysical Results of Huayingshan Fault Zone. *Earthquake Res. Shichuan* 168, 6–12. (in Chinese with English abstract). doi:10.13716/j.cnki.1001-8115.2018.03.002

Yi, G. X., Long, F., Liang, M. J., Zhao, M., and Wang, S. W. (2019). Focal Mechanism Solutions and Seismogenic Structure of the 17 June 2019 Ms 6.0 Sichuan Changning Earthquake Sequence. *Chin. J. Geophys.* 62 (9), 3432–3447. (in Chinese with English Abstract). doi:10.6038/cjg2019N0297

Yin, X. X., Guo, A. N., Zhao, T., and Li, S. H. (2019). Characteristics of the Regional Tectonic Stress Field of the Changning Ms 6.0 Earthquake, Sichuan Province. *China Earthquake Eng. J.* 41 (5), 1215–1220. (in Chinese with English Abstract). doi:10.3969/j.issn.1000–0844.2019.05.1215

Zhao, D., Qu, C., Shan, X., Gong, W., Zhang, Y., and Zhang, G. (2018). InSAR and GPS Derived Coseismic Deformation and Fault Model of the 2017 Ms7.0 Jiuzhaigou Earthquake in the Northeast Bayanhar Block. *Tectonophysics* 726, 86–99. doi:10.1016/j.tecto.2018.01.026

Zhou, R. J., Tang, R. C., Qian, H., Wen, D. H., Ma, S. H., He, Y. L., et al. (1997). An Application of Seismotectonic Analogy to the Huyingshan Fault Zone in East Sichuan. *J. Seimological Res.* 20, 316–322. (in Chinese with English abstract).

Zuo, R., Qu, C., Shan, X., Zhang, G., and Song, X. (2016). Coseismic Deformation fields and a Fault Slip Model for the Mw7.8 Mainshock and Mw7.3 Aftershock of the Gorkha-Nepal 2015 Earthquake Derived from Sentinel-1A SAR Interferometry. *Tectonophysics* 686, 158–169. doi:10.1016/j.tecto.2016.07.032

Conflict of Interest: The authors declare that the research was conducted in the absence of any commercial or financial relationships that could be construed as a potential conflict of interest.